Coherence in ultrafast laser-induced periodic surface structures

Hao Zhang,[1,*] Jean-Philippe Colombier,[1] Chen Li,[1,2,3] Nicolas Faure,[1] Guanghua Cheng,[2] and Razvan Stoian[1,†]
[1]*Laboratoire Hubert Curien, UMR 5516 CNRS, Université de Lyon, Université Jean Monnet, 42000 St. Etienne, France*
[2]*State Key Laboratory of Transient Optics and Photonics, Xian Institute of Optics and Precision Mechanics, CAS, 710119 Xian, Shaanxi, China*
[3]*University of Chinese Academy of Science, 10049 Beijing, China*
(Received 21 July 2015; revised manuscript received 1 October 2015; published 13 November 2015)

Ultrafast laser irradiation can trigger anisotropically structured nanoscaled gratinglike arrangements of matter, the laser-induced periodic surface structures (LIPSSs). We demonstrate here that the formation of LIPSS is intrinsically related to the coherence of the laser field. Employing several test materials that allow large optical excursions, we observe the effect of randomizing spatial phase in generating finite domains of ripples. Using three-dimensional finite-difference time-domain methods, we evaluate energy deposition patterns below a material's rough surface and show that modulated pattern, i.e., a spatially ordered electromagnetic solution, results from the coherent superposition of waves. By separating the field scattered from a surface rough topography from the total field, the inhomogeneous energy absorption problem is reduced to a simple interference equation. We further distinguish the contribution of the scattered near field and scattered far field on various types of inhomogeneous energy absorption features. It is found that the inhomogeneous energy absorption which could trigger the low-spatial-frequency LIPSSs (LSFLs) and high-spatial-frequency LIPSSs (HSFLs) of periodicity $\Lambda > \lambda/\mathrm{Re}(\tilde{n})$ are due to coherent superposition between the scattered far field (propagation) and the refracted field, while HSFLs of $\Lambda < \lambda/\mathrm{Re}(\tilde{n})$ are triggered by coherent superposition between the scattered near field (evanescent) and the refracted field. This is a general scenario that involves a topography-induced scattering phenomenon and stationary evanescent fields, being applied to two model case materials that exhibit large optical excursions upon excitation (W, Si) and nonplasmonic to plasmonic transitions. We indicate the occurrence of a general light interference phenomenon that does not necessarily involve wavelike surface plasmonic excitation. Finally, we discuss the role of interference field and scattered field on the enhancement of LIPSSs by simulating interpulse feedback effects and provide the electromagnetic origin of grooves ($\Lambda > \lambda$) related to a feedback-driven topography evolution. Those results strongly suggest the electromagnetic interpretation of LIPSSs in interplay with an evolving surface topography.

DOI: 10.1103/PhysRevB.92.174109 PACS number(s): 79.20.Ds, 42.25.Kb

I. INTRODUCTION

Radiation-induced organization of matter is a key issue in understanding nonstandard physical transformations of materials [1,2]. Topographical restructuring of surfaces is discernible in a wide range of natural manifestations, where stationary solutions for equations describing the evolution of dynamic systems are found in the presence of field gradients and feedback mechanisms [3–6]. Major concepts such as self-structuring, self-assembling, or self-organization imply evolutions nonachievable with linear systems and require regulating feedback. Among all these phenomena, a specific class is determined by intense light fields as the resulting structures show light localization beyond diffraction limit and a real potential of nanostructuring by optical means. Laser-induced periodic surface structures (LIPSSs), since the first observation by Birnbaum using a ruby laser in 1965 [7], attracted growing interest from both the fundamental and application points of view and they have been observed in a variety of materials [8–12]. This observation implies that regular patterning of surfaces occurring under exposure with ultrafast laser irradiation is a quasiuniversal manifestation of an intriguing matter reorganization potential. Typical examples of LIPSSs, also referred as ripples, are given in Fig. 1, showing a range of orientations and periodicity as a function of the driving field and dose (different ripple patterns that will be discussed here are marked on the figure). The LIPSS similitude with nanopatterns generated by other forms of irradiation (e.g., ion beams) or with natural upscaled phenomena shows the complexity of the phenomenon, putting forward the challenge of bringing together coherent irradiation-related features and noncoherent growth mechanisms. The particular drive for the regular displacement of matter is subject of intense efforts as it impacts cost-effective nanofabrication recipes with resolutions beyond the diffraction limit. Their control and the potential upscale in uniformity, periodicity, or effective areas is becoming determinant for a range of forecasted applications related to upgraded functions in surface engineering and nanoscale devices [13–15]: from wettability control to tribological functions, from optical marking to secure coding of information, where laser-driven nanostructuring with lithographylike quality can become competitive. Therefore, the question of the driving force behind large-scale regular nanostructuring is of paramount interest, as moreover different scenarios from plasmon activation to eigenmodes of reorganizing destabilized matter in evolution are under debate. Stipulating an optical drive, LIPSSs are strongly dependent on material properties via dielectric permittivity and laser irradiation conditions such as polarization, angles of incidence, and fluence [10,16–18]. When ripples are formed with linearly polarized laser radiation at normal incidence, their orientation could be either orthogonal or parallel to the polarization. Ripples with a periodicity close to the radiation wavelength and orthogonal to the polarization are usually referred as low-spatial-frequency

*zhterran@qq.com
†razvan.stoian@univ-st-etienne.fr

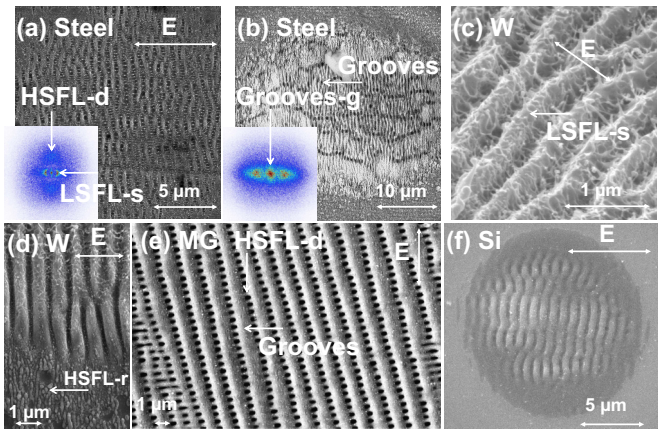

FIG. 1. (Color online) Ripple patterns on various materials: (a), (b) Stainless steel at low and high irradiation dose, (c), (d) tungsten, (e) metallic glass (data from Ref. [35]), and (f) silicon. The insets indicate relevant Fourier spectra with pointing out several classes of ripples.

LIPSSs (LSFLs) [8,10]. Sipe *et al.* established 30 years ago a pioneering comprehensive first-principles electromagnetic theory for LIPSSs formation by modeling the effect of surface roughness on the electromagnetic field [19], also known as the efficacy theory. This optical frame, with a large acceptance today, stipulates that LSFLs are formed by the inhomogeneous energy absorption due to the interference between surface scattered light and the incident light [9–11,18,20–23], and the topography-driven field superposition equally initiates the feedback mechanism [6,24]. The material response after light absorption may also contribute to LIPSS formation through electron-phonon relaxation and surface flow [25–27]. With the advancements of femtosecond laser material processing, ripples with a periodicity significantly smaller than the laser wavelength, either orthogonal [8–10] or parallel [9,11] to the polarization, have been observed and gained increasing interest. These are often referred as high-spatial-frequency LIPSSs (HSFLs). The origin of the HSFLs is still under debate in the literature, although Sipe's efficacy theory predicts the presence of electromagnetic coupling features which could explain HSFLs parallel to the polarization [9,10,19], interpretations both in the framework of electromagnetic theory [9–11,28] and mechanisms based on self-organization and surface instabilities were reported [29–31]. Very recently, in the work of Skolski *et al.*, the authors adopted the finite-difference time-domain (FDTD) method to study the inhomogeneous energy absorption below a material's rough surface [32] and feedback mechanisms [28] in the formation of LIPSSs. Significantly, it was found that HSFLs orthogonal to the polarization can be understood in the framework of electromagnetic theory. However, the origin of HSFLs and LSFLs remains yet to be discussed. Specifically, whether HSFLs can be explained by the interference between the surface scattered wave and the incident wave has not been clearly addressed so far. Furthermore, although it is intuitively accepted that LSFLs are due to the interaction between the surface scattered wave and the incident wave, our approach elucidates the critical role of coherent superposition on the formation of LIPSSs by reducing the issue to a simple interference equation. Third, although Sipe's efficacy theory already pointed out that the energy absorption feature which could lead to the development of LSFLs does not necessarily involve surface plasmon polaritions (SPPs) [19], and recently Skolski's FDTD simulation shows that SPP is not a necessary condition for the development of LSFLs [28,32], claims that SPP plays a determinant role in the formation of LSFLs are widely found in the literature [12,21,24,33,34], with a tendency to a general acceptation of its dominance. We further confirm here that the contribution of SPPs is not a necessary condition and thus not determinant for ripple formation and reinforce thus the original idea of a general optical scattering phenomenon.

In this paper, we focus on the effect of the light coherence on the generation of regular nanoscaled patterns of energy absorption. Experimentally, we study the role of randomizing phase in defining ripples. In electromagnetic calculus based on the FDTD simulations, we separate the contribution of scattered far field and scattered near field on the formation of LSFLs and HSFLs. By retrieving the scattered field, the problem of inhomogeneous energy absorption is reduced to a simple interference equation. It is found that the inhomogeneous energy absorption which could trigger the LSFLs and HSFLs with periodicity $\Lambda > \lambda/\mathrm{Re}(\tilde{n})$ [HSFLs with $\Lambda < \lambda/\mathrm{Re}(\tilde{n})$] are due to inherently coherent superposition between the scattered far field (scattered near field) and the usual refracted field, although for plasmonic metals, the energy absorption due to the scattered field alone can show preferential directions. Second, we further confirm the fact that plasmonic-active character of materials is not a necessary condition which must be satisfied for the formation of LSFLs. Besides, we quantify the influence of SPPs in the formation of LSFLs. Finally, we discuss the interpulse feedback mechanism on the enhancement of the ripple pattern and the origin of the grooves. Both of these findings strongly support the electromagnetic interpretation of the physical mechanisms underlying the formation of LIPSSs.

II. TUNING COHERENCE AND PHASE PATTERNS OF THE FIELD

The question of spatial coherence or phase distribution of an optical field is key in understanding light-induced phenomena [36]. We therefore tested the effect of a randomized phase and its supposed effect on spatial coherence using ultrafast laser pulses. We principally used an ultrafast (50 fs, 800 nm) laser irradiation source to expose metallic stainless steel surfaces. A ground glass diffuser is used to imprint a random phase across the incoming beam. It is nevertheless to be observed that, due to the short pulse duration, the requirement for decreasing the spatial coherence by the temporal randomness between the field at two transverse positions is not fully fulfilled and the pulse is too short to experience decrease in the spatial degree of coherence. In the case of a single pulse, the ground plate will scatter light with a quasiarbitrary phase in the transverse direction. This phase distribution creates scattering effects, i.e., speckle. In case of pulse trains, the situation is different and two cases may be observed. First, one involves a still diffuser plate, resuming essentially to the single-pulse case where no time randomness of the phase is achieved and the phase does not change from pulse to pulse. The second case involves a moving diffuser plate, affecting

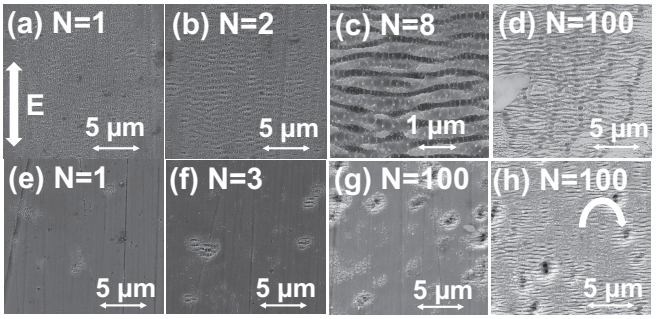

FIG. 2. Irradiation results in stainless steel. (a)–(d) Irradiation with Gaussian spatially coherent smooth-phased ultrafast laser beams resulting in ripple formation at various incident pulse number in the vicinity of the modification threshold. (e)–(h) Irradiation with random-phased ultrafast laser beams resulting in ripple formation at various incident pulse number. (e), (f) Describe the case of a static plate at low number of shots per site, emphasizing the speckle effect. (g), (h) Compare the situation for a given number of pulses per site ($N = 100$) for a static and a moving plate, i.e., coherent and partially coherent pulse train.

the time-averaged correlation between two arbitrary locations within the beam section for a time domain much longer than a single laser pulse and implying multishot sequences. Each single pulse in the train experiences a static ground glass plate, but during the duration of the pulse sequence the plate is rotating, applying a different phase distribution in the transverse direction for each pulse (and hence different speckle pattern). The temporal averaging in each spatial position (or in the far zone) reveals that the field has become partially coherent, with single-pulse effects being random phased but spatially coherent. Irradiation results are given in Figs. 2(a)–2(h). The figure depicts a comparison between the results induced by collimated Gaussian coherent beam [Figs. 2(a)–2(d)] at increasing dose and the random-phased beams [Figs. 2(e)–2(h)], a comparison that targets the spatial localization of ripples pattern. The case of a static or moving phase with its effect on the spatial coherence of a pulse train is also described [Figs. 2(g) and 2(h)]. The Gaussian exposure delivers the expected ripple pattern with spatial frequency components either perpendicular or parallel to the field, extending over the spatial domain of the beam. However, in the case of a randomized phase, contrary to the case of the Gauss beam, where the area is uniformly covered with ripples, the employment of static diffuser delivers local domains of ripples with characteristic sizes approaching the diffraction limit, corresponding to an expected speckle pattern. No conclusion can be gathered if the discrete pattern is related to a threshold condition achieved on the speckle pattern or to the local interference conditions between the incoming wave vectors. Noteworthy, the employment of a rotating diffuser during multipulse ($N = 100$) sequence shows a higher degree of filling with rippled patterns, originating from a time average of the speckle pattern. Interesting, although the phase character is randomized from pulse to pulse, a certain continuity between the rippled patterns is to be observed, indicating two points: the potential role of a corrugated topography and its part in initiating feedback. To elucidate the role of spatial-temporal coherence, we investigated a set of numerical conditions that offer a representative picture of the experimental patterns observed on femtosecond laser-irradiated samples.

III. FDTD STUDY OF THE FORMATION OF LIPSS

A. FDTD method

With the progress in calculation power, the FDTD method introduced by Yee in 1966 [37] has gained increasing popularity to numerically solve the Maxwell equations. By introducing the dielectric function ϵ_r, the two curl operator in the Maxwell's equations can be written as [38,39]

$$\frac{\partial \mathbf{H}}{\partial t} = -\frac{1}{\mu_0}\nabla \times \mathbf{E}, \tag{1}$$

$$\frac{\partial \mathbf{D}}{\partial t} = \nabla \times \mathbf{H}, \tag{2}$$

$$\mathbf{D}(\omega) = \epsilon_0 \epsilon_r(\omega)\mathbf{E}(\omega), \tag{3}$$

where t is the time, μ_0 is the vacuum permeability, ϵ_0 is the vacuum permittivity, $\mathbf{E}$ is the electric field, and $\mathbf{H}$ is the magnetic field. In the FDTD method, central differences scheme in a Cartesian frame is used for the spatial curl operators and the time derivatives. Note that the displacement field $\mathbf{D}$ is expressed in the frequency domain. This allows us to more conveniently treat dispersive and lossy materials as in the case of metals with a negative permittivity by using the auxiliary differential equations (ADE) method [38]. The equations march through time by a so-called leapfrog arrangement, in a way that each component of $\mathbf{D}$ and thus $\mathbf{E}$ is updated and stored using previous components of $\mathbf{H}$, and all $\mathbf{H}$ components are updated from $\mathbf{E}$ and the cycle starts again. Apart from choosing Δx to be adequately small to resolve the problem, the numerical stability of Yee's algorithm in three dimensions requires the Courant condition [38], i.e., $\Delta t \leqslant \Delta x/\sqrt{3}c$, where c is the speed of light in free space and Δt the time step. In order to numerically solve the equations, central differences scheme in a Cartesian frame is used for the spatial curl operators and the time derivatives.

B. Inhomogeneous energy deposition below a rough surface

In this section, we employ the FDTD method to study the periodic energy deposition below a material's rough surface. A schematic of the simulation domain is shown in Fig. 3. To construct a rough surface in FDTD, we describe the dielectric function of the top layer of the simulated material by a two-value function $\epsilon_r(y,z)$ [32], i.e.,

$$\epsilon_r(y,z) = \epsilon_2, \quad \text{for the filled region,}$$

$$\epsilon_r(y,z) = 1, \quad \text{for the unfilled region,}$$

where ϵ_2 is the dielectric function of the simulated material. One can use another binary function $B(y,z)$ to define a so-called filling factor, that is, for the filled region, $B = 1$, otherwise, $B = 0$. The filling factor F is then the mean value of function $B(y,z)$ over all the FDTD cells in the roughness layer. In the simulations concerning multiple rough particles in this paper, F was set to 0.2. The dimension of the rough particles is set to 20 nm × 20 nm × 20 nm throughout the paper unless specified. Above the roughness layer, it is the source plane (embedded in air) where a soft source [38] in air is injected

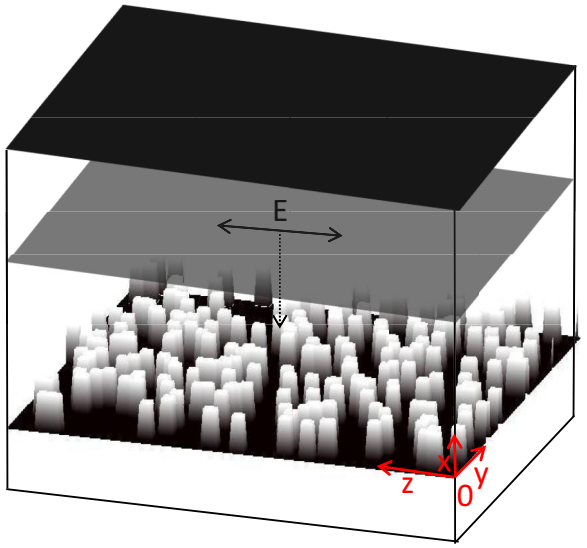

FIG. 3. (Color online) Schematic of the FDTD computation domain of a randomly distributed binary rough surface. Note that the image is not to scale. The gray plane is the position where the incident wave (a quasi-plane-wave) is sent. The double-sided arrow illustrates the direction of the polarization of the incident pulse. The perfectly matched layer (PML) is not shown in the figure, but in simulations the computation domain is completely enclosed by PML regions in all directions. The $x = 0$ plane is defined as the plane immediately below the roughness layer.

into the computation grid. We use the electric field component E_z as the soft source, thus presenting an EM wave polarized in z direction (see Fig. 3) and traveling downward towards the material surface at normal incidence. Throughout all the simulations performed in this paper, we use linear-polarized light as the incident source whose electric vector is pointing in the z direction. The instantaneous value of the source is computed following the electric field value of a $\tau = 30$ fs laser pulse (wavelength $\lambda = 800$ nm) with a Gaussian envelope in time, where τ is the FWHM pulse duration. This pulse duration $\tau = 30$ fs was chosen such that one can get a steady-state solution (the spatial distribution of the inhomogeneous energy absorption is not changing over time when the simulation is about to end), and on the same time, the simulation will be performed in a reasonable amount of time. The peak intensity at each FDTD cell of the source is determined by assuming the fluence distribution is a super-Gaussian type of order 7. This super-Gaussian distribution is employed to form a quasi-plane-wave and to maximize the interaction area between the incident pulse and the rough surface. Note that one can set the super-Gaussian order to 2, thus simulating a real focused laser pulse. To minimize nonphysical reflections at the boundaries, the computation domain is fully enclosed by perfectly matched layers (PML) in all the six directions. In each boundary, the thickness of the PML is $7\Delta_x$. The lateral dimension ($N_y\Delta_x$ and $N_z\Delta_x$) of the simulation domain is large enough to contain at least several wavelengths of the laser radiation, where N_y and N_z are the number of FDTD cells in the y and z directions. The number of FDTD cells in the x direction N_x was set to 25. The structure being simulated was constituted by six layers, thus the energy absorption can be studied deep into the material. In all the calculations performed in this paper, Δ_x was set to 20 nm. The FDTD time step was set to 0.033 fs, satisfying the Courant condition. Above the roughness layer ($x > \Delta_x$), there are three layers of vacuum. The complex amplitude of the electric fields $\widetilde{E_0}$ was computed once half an optical cycle and for each FDTD cell, using the time-varying field value obtained directly from the FDTD simulation [40]. From the complex amplitude, the energy dissipation rate Q in each FDTD cell is determined with [39]

$$Q = \frac{1}{2} c\epsilon_0 \frac{4\pi \mathrm{Im}(\widetilde{n})}{\lambda} \mathrm{Re}(\widetilde{n}) |\widetilde{E_0}|^2, \tag{4}$$

where λ is the wavelength in free space, $\widetilde{n}$ is the complex refractive index. An integration of Q over the simulation duration yields the absorbed energy density $\xi = \int_{-\infty}^{\infty} Q\, dt$. To study the energy absorption in frequency domain, a two-dimensional fast Fourier transform (FFT) was performed to the absorbed energy density ξ in (y,z) planes below the rough surface. The simulation is performed for three types of material states, namely, dielectric, metallic material with a plasmonic-inactive permittivity [$\mathrm{Re}(\epsilon_r) > -1$], and metallic material with a plasmonic-active permittivity [$\mathrm{Re}(\epsilon_r) < -1$, which supports the propagation of surface plasmon polariton]. Two test materials are used fulfilling the above conditions under excitation, silicon (Si) and tungsten (W), as they show large excursion of optical properties during laser excitation and particular nonplasmonic to plasmonic state transitions driven by electronic excitation. Other materials are used on a punctual manner. A benchmark of our self-developed FDTD code we use to do the calculations presented in this paper can be found elsewhere [40].

Figure 4 shows the absorbed energy density ξ_z contained in the electric field component E_z (y,z) at planes below the roughness layer and their Fourier transform in unexcited silicon (refractive index $\widetilde{n} = 3.7 + 0.0065i$) and excited silicon (carrier density $N = 3 \times 10^{21}$ cm^3 with refractive index $\widetilde{n} = 2.4 + 0.68i$). The noise in this figure comes from the fact that the simulation was performed with a randomly distributed rough surface. The refractive index of excited silicon is calculated using the Drude model with a carrier-carrier collision time $\tau_d = 1.1$ fs and carrier effective mass $m^* = 0.18m_e$, where m_e is the electron rest mass [41]. The results are given at different (y,z) planes below the roughness layer. We mainly consider the absorbed energy contained in E_z component (the same axis as the polarization direction of the incident pulse). The reason comes from two facts observed in the FDTD simulations. One reason is that the E_z field has the largest strength, the other reason is that, for most cases, the other two components do not show significant preference in the directions of the periodic energy absorption as compared with the z component, however, in some particular conditions, they do show preferential direction in the absorbed energy and this will be discussed later in the paper. It should be noted that our results agree well with the study by Skolski *et al.* [32] in which similar calculations were first performed. Indicated by localized domains in the Fourier space, we observe in Fig. 4 that they show regular features, thus, the absorbed energy has preferential directions. The preferential directions of the energy absorption are also easily be seen in Figs. 4(g) and 4(h)

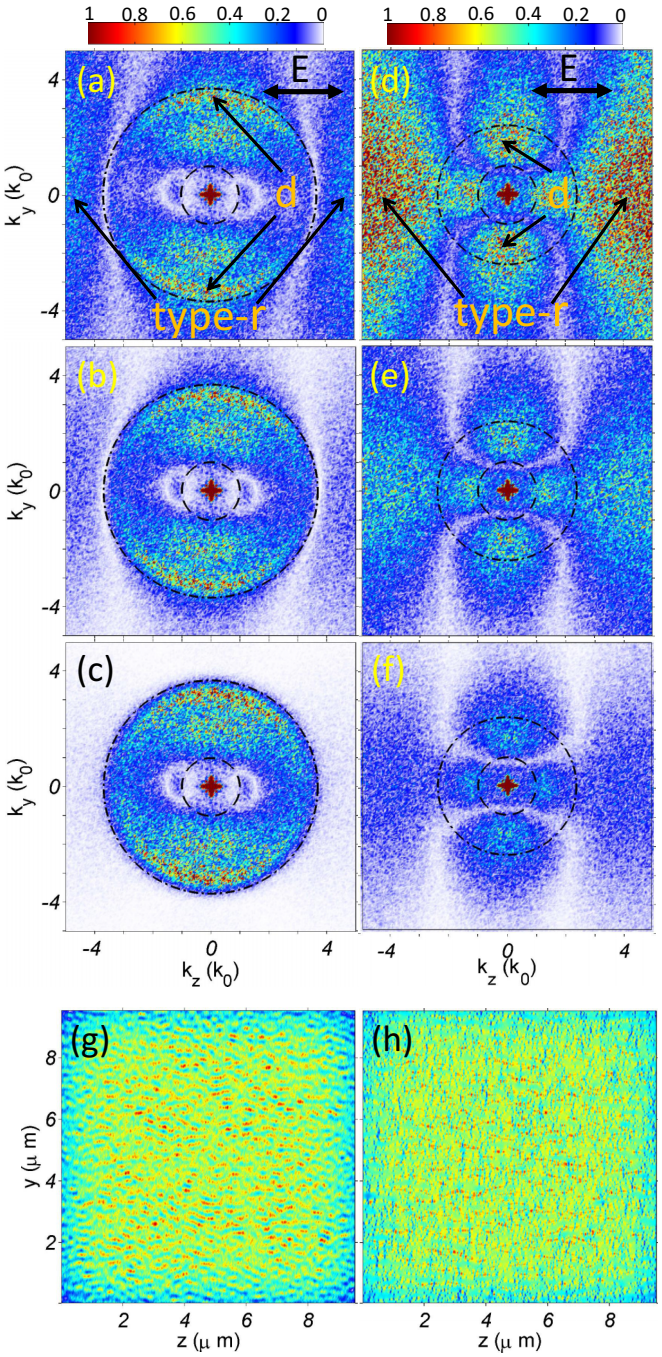

FIG. 4. (Color online) Fourier transform amplitude of the absorbed energy density ξ_z at various (y,z) plane below the roughness layer [(a), (d) $x = 0$ nm; (b), (e) $x = -20$ nm; (c), (f) $x = -40$ nm] in (a)–(c) unperturbed silicon and (d)–(f) excited silicon with carrier density $N = 3 \times 10^{21}$ cm^3, corresponding refractive index $\widetilde{n} = 2.4 + 0.68i$. The dashed-dotted and dashed circles represent $|\mathbf{k}| = \mathrm{Re}(\widetilde{n})k_0$ and $|\mathbf{k}| = k_0$, respectively, where k_0 is the free-space wave number. The polarization direction is along the z axis and indicated by the black arrow in (a) and (d). The ξ_z in real space is shown in (g) and (h) at $x = -20$ nm for unexcited and excited silicon, respectively.

which show the absorbed energy density in real space. For the sake of convenience and easy comparisons with results by other groups, we use the widely accepted terminology for those regular features found in the frequency domain. Type-d structures, as indicated in Figs. 4(a) and 4(d) (see also Fig. 1), correspond to inhomogeneous energy absorption parallel to the laser polarization with a periodicity around $\lambda/\mathrm{Re}(\widetilde{n})$ (HSFLs), where λ is the incident wavelength. Shown from Figs. 4(a) to 4(c), as we look into deeper layers inside the material, the outer part of the circle $|\mathbf{k}| = \mathrm{Re}(\widetilde{n})k_0$ of the type-d feature vanishes while the inner part becomes more pronounced. The type-r feature, which corresponds to HSFLs perpendicular to polarization, can also be seen. Similar to the outer part of the type-d feature, as shown from Figs. 4(a) to 4(c) and from Figs. 4(d) to 4(f), the type-r feature gradually loses its intensity at greater depth. It is proposed here that the formation of the type-r feature and the outer part of the type-d feature are caused by the coherent superposition (the role of interference between the scattered field and the usual refracted field will be discussed in the following sections) between the scattered near field which has an in-plane [the (y,z) plane] wave-vector magnitude $k_{\parallel}$ larger than $\mathrm{Re}(\widetilde{n})k_0$ and the usual refracted field. By the scattered field, we refer to the field that is scattered by individual roughness particles. If one decomposes the total wave vector of the scattered field $\mathbf{k}_{sca} = \mathrm{Re}(\widetilde{n})k_0\widehat{\mathbf{k}}$ into parallel and normal components, where $\widehat{\mathbf{k}}$ is a unit vector, one finds

$$k_{\perp}^2 = [\mathrm{Re}(\widetilde{n})k_0]^2 - k_{\parallel}^2 < 0. \quad (5)$$

Since for those wave vectors responsible for the type-r feature and the outer part of the type-d feature, their magnitude $k_{\parallel} > \mathrm{Re}(\widetilde{n})k_0$, thus, $k_{\perp}$ is purely imaginary. Therefore, the scattered field which forms (through coherent superposition with the usual refracted field) the outer parts of the type-d feature and the type-r feature will evanescently decay over greater depth, as observed in Fig. 4.

Upon fs laser excitation of tungsten, the electron cloud absorbs the energy and thermalizes to an elevated temperature while the lattice remains cold during the laser pulse. We therefore use the dielectric constant of tungsten at $T_e = 25\,000$ K calculated by *ab initio* simulations to account for the change of optical properties during the excitation process. The *ab initio* simulations suggest a nonplasmonic to plasmonic transition at this elevated temperature [42]. The properties will evolve from the typically cold nonplasmonic state [$\widetilde{n} = 3.6 + 2.8i$ corresponding to $\epsilon_r = 5.35 + 20i$, with $\mathrm{Re}(\epsilon_r) > -1$] to a state with negative permitivitty where resonant surface plasmonic excitation conditions are fulfilled by the characteristic optical indices ($\widetilde{n} = 2.1 + 3.9i$ corresponding to $\epsilon_r = -10.5 + 16.4i$). Figure 5 shows the absorbed energy density and their Fourier transform in tungsten with electron temperature $T_e = 300$ K ($\epsilon_r = 5.35 + 20i$) [43] and tungsten with electron temperature $T_e = 25\,000$ K ($\epsilon_r = -10.5 + 16.4i$) [42]. These two material states can be treated as representatives of plasmonic-inactive and plasmonic-active materials. As shown in Figs. 5(a) and 5(b), both plasmonic-inactive and plasmonic-active materials show strong type-s feature, which corresponds to inhomogeneous energy absorption perpendicular to the laser polarization with a periodicity slightly smaller than λ (LSFLs). It should be noted that surface roughness does change the effective index of the material, to investigate whether surface roughness can alter the effective index of nonplasmonic tungsten from plasmonic-inactive type to plasmonic-active type, we have calculated the effective index of tungsten with $T_e = 300$ K

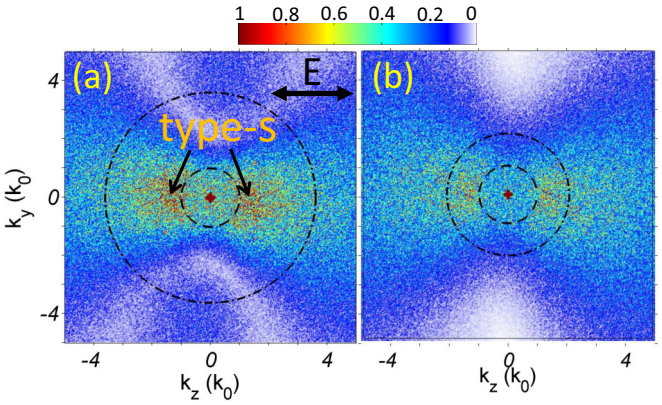

FIG. 5. (Color online) Fourier transform amplitude of the absorbed energy density ξ_z in (y,z) plane of $x = -20$ nm for (a) tungsten with electron temperature of $T_e = 300$ K, dielectric constant $\epsilon_r = 5.35 + 20i$ and (b) tungsten with $T_e = 25\,000$ K, dielectric constant $\epsilon_r = -10.5 + 16.4i$.

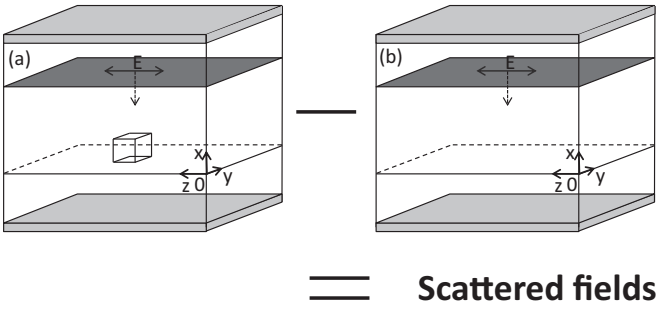

FIG. 6. Sketch of the numerical determination of the field scattered by a single rough particle (the scattered field). The difference in the time-varying field values between (a) simulation with a single rough particle and (b) simulation with no roughness gives the field scattered by that single rough particle. Note that the method can be equally adopted for the determination of the field scattered by multiple rough-particles.

which has surface roughness as shown in Fig. 3. Specifically, by using the FDTD method, we calculated the reflectivity and transmissivity at normal incidence of a 40-nm layer nonplasmonic tungsten (sandwiched by air) with the presence of surface roughness following the geometry shown in Fig. 3. From the calculated reflectivity and transmissivity of the rough structure and by using the analytical transfer-matrix model which can solve the reflectivity and transmissivity of smooth layered structures [39], one can extract by which effective index a smooth structure with the same thickness calculated by the transfer-matrix model yields the same reflectivity and transmissivity as the rough structure calculated by the FDTD, thus providing the effective optical index of the latter. Note that we have tested this method by calculating the effective index of a 40-nm smooth layer of nonplasmonic tungsten which yields its correct (original) value. The results show that the effective optical index of tungsten at $T_e = 300$ K with a rough surface following Fig. 3 (with a filling factor $F = 0.2$) is $\widetilde{n_{\text{eff}}} = 3.3 + 2.3i$, with a decrease in both the real and imaginary parts of $\widetilde{n}$ comparing to the original value $3.6 + 2.8i$. But, it is still plasmonic inactive, therefore along the conclusions in Refs. [19,32], we further confirm here that a plasmonic-active material [$\text{Re}(\epsilon_r) < -1$] is not a necessary condition that must be satisfied for the LSFLs formation. The role of plasmonic-active optical property on the scattered field and its coherent superposition with the refracted field will be discussed in the following sections.

C. Scattered field

Are the inhomogeneous energy depositions (type-s, type-d, and type-r) we calculated in the previous section caused by the interference between scattered wave due to surface roughness and the usual refracted wave? What is the role of plasmonic-active and plasmonic-inactive materials on the formation of LSFLs (type-s features)? To shed light on these questions, it is helpful to look at the scattered field only. In order to achieve this, from the electric fields calculated by the FDTD simulations, we separated the scattered field from the total fields. The method is illustrated in Fig. 6. We first run FDTD simulation under the presence of a single rough particle on the material's surface, after that we run simulation with no roughness presence. The size of the rough particle is 100 nm × 100 nm and it has a thickness of 20 nm. The location of the rough particle is on the center of the material's surface. Thanks to the superposition principle, the electric fields value difference between the two simulations yields the value of the scattered field caused by that single rough particle. It should be noted that the electric fields here are the time-varying $E_{zs}(y,z,t;x)$ fields at a depth of $x = 0$ nm contained in the last optical half-cycle of the FDTD simulations. This is because half an optical cycle is the minimum period which is required to have the complete information about the steady-state field (the phase and the amplitude). The reason we choose the last half-cycle is that it is the most numerically stable one (and perhaps physically also). We use the subscript z to indicate that the field is the z component and the subscript s refers to the scattered field.

We show in Fig. 7 the amplitude and phase of the scattered field (by a single rough particle) which are extracted from the time-varying field values using the method discussed in Ref. [40]. The cross-section values of the phase are shown in Fig. 7(d). We can see that inside the region indicated by the two vertical green dashed lines, the phase takes the form of a complex function, while beyond this region, the phase is a linear function of the propagation distance (note that $-\pi$ and π are the same phase). This means that the region beyond the two green dashed lines is the far field because the phase of a propagation wave (far field) is a linear function of the propagation distance ($k_z z$ or $k_y y$). The region within the two green dashed lines is then the near field (evanescent). As shown in Fig. 7(c), the field amplitude value in the two regions has different dependency on the propagation distance. This is also a noteworthy corroboration of the determination of the near-field and far-field regions [44]. From the distance between the two vertical green dashed lines, it is determined that in this particular case studied, the near-field region has a radius of 220 nm.

Figures 8(a)–8(f) show the Fourier transform amplitude of the scattered field at various time moments during half an optical cycle. This Fourier spectrum provides us information

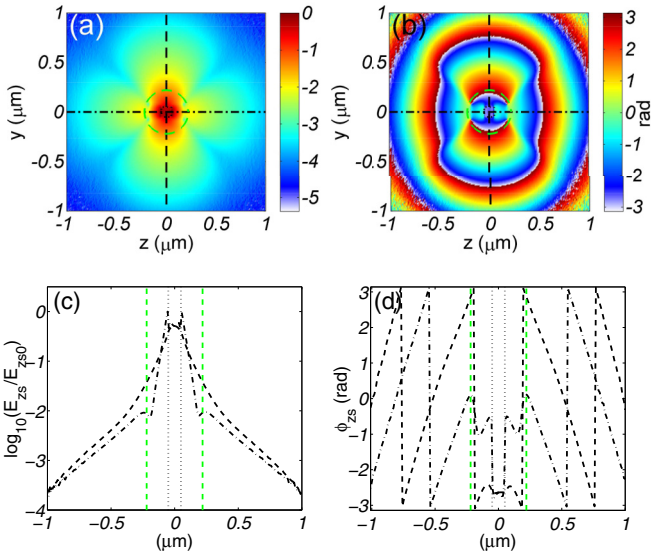

FIG. 7. (Color online) The logarithm of the normalized amplitude (a) and the phase (b) of the field scattered by a single rough particle. The position and size of the rough particle are indicated by the black square (dotted line) in the middle. Their cross-section values along two orthogonal directions (dashed line for vertical and dashed-dotted line for horizontal) are shown in (c) for amplitude and (d) for phase. The green dashed line in (c) and (d) and the green dashed circle in (a) and (b) indicate the boundary between the near field and the far field. The calculation is performed for silicon with a free-carrier density of $N = 3 \times 10^{21}$ cm^3 and corresponding refractive index $\tilde{n} = 2.4 + 0.68i$.

on which wave vectors of the scattered field are particularly strong [44]. The calculation was performed for silicon with a free-carrier density of $N = 3 \times 10^{21}$ cm^3 and refractive index $\tilde{n} = 2.4 + 0.68i$. This carrier density is chosen such that both type-s and -d features are more or less equally pronounced in the Fourier spectrum so both features can be analyzed in one calculation.

In order to specify the time coordinate during the optical half-cycle, we use the field value in the center of the (y-z) plane (so it is also the center of the rough particle) to indicate the relative time position during the cycle. For example, Fig. 8(a) shows the Fourier transform amplitude of the scattered field at the moment when the field value in the center E_{zsc} reaches its amplitude value E_{zsc0}. We define this time moment as $t = 0$. The pattern of the Fourier transform repeats itself every half an optical cycle as Fig. 8(f) is identical to Fig. 8(a). The type-s feature becomes the most pronounced when the electric field in the center reaches its maximum value, i.e., when $t = 0$. It gradually loses its intensity for the following time steps. In the meantime, the intensity of the type-d feature increases and becomes the most pronounced from $t = 0.24T_{\mathrm{cyc}}$ to $t = 0.36T_{\mathrm{cyc}}$, where T_{cyc} refers to the duration of an optical cycle. The intensity increase of the type-d feature is also associated with the change of its location, i.e., when its intensity is increased, the peak of its distribution moves from the outside of the circle $|\mathbf{k}| = \mathrm{Re}(\tilde{n})k_0$ to the inside of $|\mathbf{k}| = \mathrm{Re}(\tilde{n})k_0$. The inner side and the outer side [with respect to $|\mathbf{k}| = \mathrm{Re}(\tilde{n})k_0$] of the type-d feature have different origin and we will discuss it later. Refer to the type-r feature, around $t = 0$, it is merged

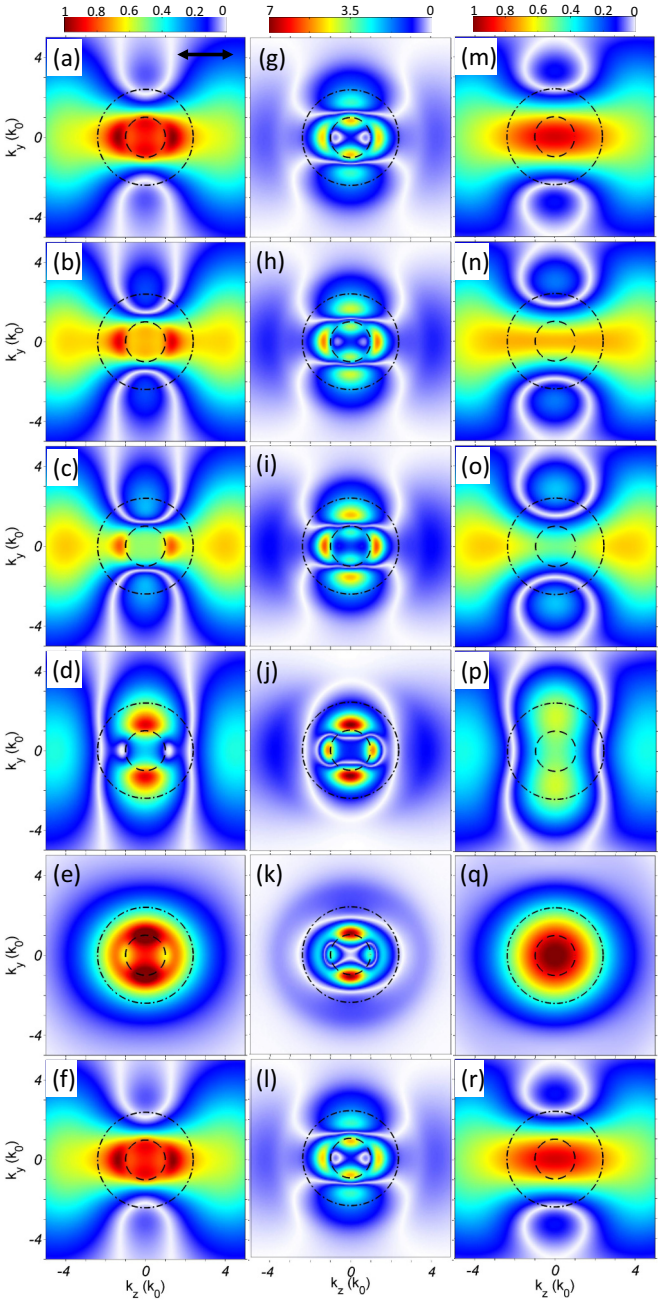

FIG. 8. (Color online) Fourier transform amplitude of the time-varying total scattered field (a)–(f), the scattered far field (g)–(l), and the scattered-near-field (m)–(r) by a single rough particle at various time moment during half an optical cycle when $t = 0$ [(a), (g), (m)], $t = 0.05T_{\mathrm{cyc}}$ [(b), (h), (n)], $t = 0.09T_{\mathrm{cyc}}$ [(c), (i), (o)], $t = 0.24T_{\mathrm{cyc}}$ [(d), (j), (p)], $t = 0.36T_{\mathrm{cyc}}$ [(e), (k), (q)], and $t = 0.5T_{\mathrm{cyc}}$ [(f), (l), (r)], at a depth of $x = 0$ nm. The calculation is performed for silicon with a free-carrier density of $N = 3 \times 10^{21}$ cm^3 and corresponding refractive index $\tilde{n} = 2.4 + 0.68i$. The color scale of each column is shown on the top.

with the type-s feature, after that, its intensity increases, around $t = 0.09T_{\mathrm{cyc}}$ it separates from the type-s feature and its intensity reaches approximately the maximum value. Although the above discussion seems to suggest that the appearance of the type-s and type-d features are separated in time, we should note that the Fourier transforms shown in Figs. 8(a)–8(f)

are strongly influenced by their near-field components. The swift phase change from the near-field region to the far-field region largely determines the time separation between the type-s and -d features in the total scattered field. We see from Figs. 7(a) and 7(c) that the near-field amplitude is much larger than the far-field amplitude, hence, the near-field component is supposed to have large influence on the Fourier transform of the total scattered field. In order to separate out their contributions, we set the far-field value (outside the green circle of a radius of 220 nm) to 0, thus representing only the contribution of the near field. The Fourier transform amplitudes of the scattered near field during half an optical cycle are then shown in Figs. 8(m)–8(r). To separate out the contribution of only the far field, we use a different approach since directly setting the near-field value to zero causes an abrupt cutting off of the field, and give rise to unwanted high-frequency components. Instead, we use a Gaussian function to gradually set the near-field values, eventually approaching 0 in the center of the near-field region. Note that in this way it is not possible to eliminate all the spectral components of the near field in the Fourier transform of the far field, but its contribution could be minimized. The Fourier transform amplitudes of the scattered far field are then shown in Figs. 8(g)–8(l). It can be seen that the appearance of type-s and -d features in the far field are approximately in phase while in the total scattered field there is a phase difference between them. Such a phase difference is caused by the swift phase change across the near-field–far-field boundary [see Fig. 7(d)]. Comparing Figs. 8(g)–8(l) with Figs. 8(m)–8(r), we can conclude the following: (1) The type-r feature and the outer part of type-d feature [outside $|\mathbf{k}| = \mathrm{Re}(\tilde{n})k_0$] only appear in the near field. (2) The type-s feature and the inner part of type-d feature [inside $|\mathbf{k}| = \mathrm{Re}(\tilde{n})k_0$] only appear in the far field. Note that the high-frequency contributions [$|\mathbf{k}| > \mathrm{Re}(\tilde{n})k_0$] in Figs. 8(g)–8(l) are the residual spectral components of the near field. It is worth noting that the same conclusion was also drawn by analyzing the energy absorption spectra at different planes below the roughness layer, i.e., Eq. (5). Note that one should distinguish the scattered wave vector shown in Fig. 8 from the absorbed energy. Nevertheless, we will show in the following section that the scattered field with those wave vectors interferes with the refracted field, leading to preferential deposition of energy. Thus, the periodical energy deposition which could trigger LSFLs (type-s) and HSFLs of periodicity $\Lambda > \lambda/\mathrm{Re}(\tilde{n})$ (inner part of type-d) are due to coherent superposition between the scattered far field (propagation) and the refracted field while HSFLs of $\Lambda < \lambda/\mathrm{Re}(\tilde{n})$ (type-r and outer part of type-d) are initiated by coherent superposition between the scattered near field (evanescent) and the refracted field.

Figure 9 shows the Fourier transform amplitude of the scattered far field in plasmonic-active (tungsten with $T_e = 25\,000$ K, $\epsilon_r = -10.5 + 16.4i$) and plasmonic-inactive (tungsten with $T_e = 300$ K, $\epsilon_r = 5.35 + 20i$) materials. They are shown for the time moment when the intensity of the type-s feature in each material becomes the most pronounced during its optical cycle. A calculation of gold with a large negative dielectric constant ($\epsilon_r = -26.2 + 2.07i$) is also shown as a typical plasmonic-active material for comparison. The Fourier transform amplitude calculated for each material is normalized by the maximum amplitude found in the case of nonplasmonic tungsten. The Fourier transform amplitudes in the line $k_y = k_0$

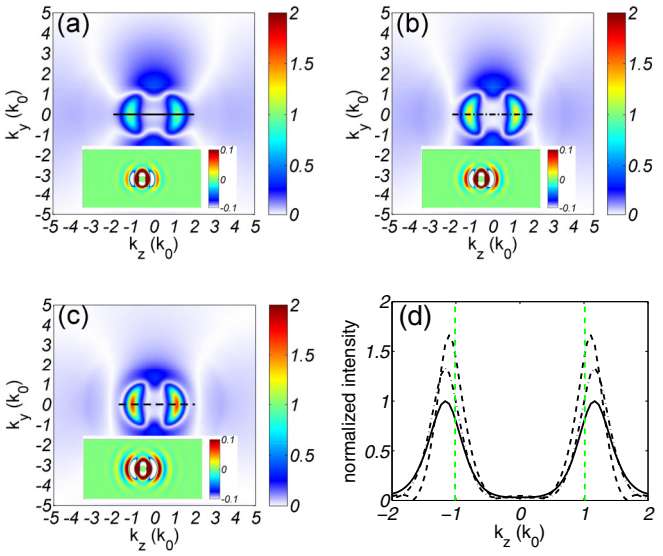

FIG. 9. (Color online) Fourier transform amplitude of the scattered far field in (a) tungsten with $T_e = 300$ K ($\epsilon_r = 5.35 + 20i$), (b) tungsten with $T_e = 25\,000$ K ($\epsilon_r = -10.5 + 16.4i$), and (c) gold ($\epsilon_r = -26.2 + 2.07i$), at the moment when the intensity of the type-s feature in each material becomes the largest during its optical cycle. The insets are the corresponding scattered-far-field distribution in real space (lateral dimension 8 μm). The Fourier transform amplitude of the type-s feature in the line of $k_y = 0$ is shown in (d) for tungsten with $T_e = 300$ K (solid line), tungsten with $T_e = 25\,000$ K (dashed-dotted line), and gold (dashed line). The two green dashed lines in (d) show the surface-plasmon wave number in plasmonic tungsten ($k_z = 1.013k_0$).

for the calculations of the three materials are shown in Fig. 9(d) for a quantitative comparison. We can see that both plasmonic-active and plasmonic-inactive materials show type-s feature in the spectrum of the scattered field, but the more negative the real part of the dielectric constant is, the stronger the type-s feature becomes, and in the meantime the spectrum peak gets closer to the surface-plasmon wave vector. This can be also corroborated by the field distributions (insets) in Figs. 9(a)–9(c), which show that even for plasmonic-inactive tungsten, there already is field scattering along the direction of polarization, while the gold shows the strongest scattering, is consistent with the above spectral analysis. The far-field scattering in the case of plasmonic-inactive materials is likely to be caused by the Mie-scattering process [45]. As we will show in the next section that the final inhomogeneous energy absorption is due to coherent superposition between the usual refracted field and the scattered field, these spectrum features in the Fourier transform of the scattered field (scattered wave vectors) is supposed to also appear in the energy absorption spectrum (indeed, the energy absorption spectrum in Fig. 5 shows type-s features for both plasmonic-active and plasmonic-inactive tungsten). Since the type-s feature represents LSFLs perpendicular to the polarization, we conclude that plasmonic-active material (supporting collective charge oscillations) is not a necessary condition for the formation of LSFLs perpendicular to the polarization, but materials with a plasmonic-active optical property enhance the formation of LSFLs.

D. Interference between scattered field and usual refracted field

Comparing Figs. 8(a)–8(f) with Fig. 4(d), the spectrum of the scattered field has similar features as the spectrum of the absorbed energy. For example, type-s, type-d, and type-r features in the Fourier transform amplitude of the absorbed energy (energy absorption spectrum) can all be found in the Fourier transform amplitude of the scattered field (the scattered wave vector). As we already pointed out, the Fourier transform of the scattered field determines which wave vectors of the scattered field are particularly strong. Therefore, could it be that the energy spectrum features (type-s, type-d, type-r) are due to coherent superposition between the usual refracted field with the scattered field which has already had those wave vectors? To answer this question, recall that by running the simulations with and without the roughness (Fig. 6), we already obtained the time-varying values of the scattered field for the last optical half-cycle (Fig. 8). From those time-varying field values, we could extract the amplitude and phase of the scattered field using the method discussed in Ref. [40]. They are shown in Fig. 7, where the amplitude is normalized by their maximum value in the plane considered. Similarly, the amplitude and phase of the usual refracted field can also be extracted from the time-varying field values of the simulation performed without the presence of any roughness (smooth sample surface). Having both the amplitude and phase of the scattered field and refracted field, it is very straightforward to calculate the intensity of the interference $I_{\rm tot}$ between the scattered field and the refracted field by the simple interference equation [36,39]

$$\begin{aligned} I_{\rm tot} &= I_{zr} + I_{zs} + 2\sqrt{I_{zr} I_{zs}}\,{\rm Re}[\gamma(\mathbf{r_1},\mathbf{r_2},\tau)] \\ &= I_{zr} + I_{zs} + 2\sqrt{I_{zr} I_{zs}}\cos[\phi_{zr} - \phi_{zs}] \\ &= I_{zr} + I_{zs} + I_{zi}, \end{aligned} \tag{6}$$

where I_{zr}, I_{zs}, and I_{zi} refer to the intensity of the refracted field, the scattered field and the intensity of the field caused by the last (interference) term which is strongly related to the definition of coherence via the complex degree of coherence γ [36]. The symbols ϕ_{zr} and ϕ_{zs} represent the phase of the refracted field and the scattered field, respectively. By the term "refracted field" or "usual refracted field" in the paper, we refer to the incident electromagnetic field below a smooth sample surface with no presence of the roughness layer. Figure 10(a) shows the Fourier transform of the field intensity directly obtained from FDTD simulations with the presence of a single roughness particle while the Fourier transform of the total field recovered by Eq. (6) is plotted in Fig. 10(b). As a comparison, the Fourier transform of the field intensity by only the scattered term I_{zs} or only the interference term I_{zi} of Eq. (6) is also shown in Figs. 10(c) and 10(d). As can be seen, the scattered field itself [shown in Fig. 10(c)] does not give rise to strong preferential direction in the field intensity, it is the interference term [shown in Fig. 10(d)] which produces periodic energy absorptions. The Fourier transform of the refracted-field term I_{zr} is not shown in Fig. 10. However, in Figs. 10(a) or 10(b), its contribution can be seen close to the origin (inside the circle $|\mathbf{k}| < k_0$). We should note that the analyzing about energy absorption and the scattered field by only a single rough particle also applies to the case of multiple random roughness. This is because

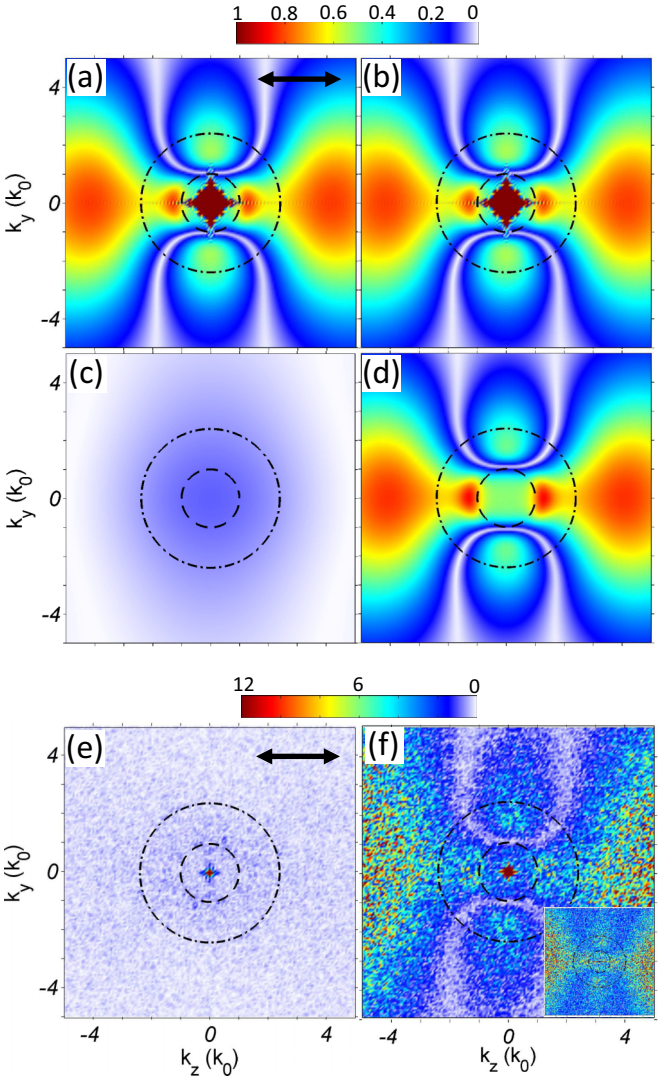

FIG. 10. (Color online) Fourier transform amplitude of (a) the total-field intensity obtained directly by FDTD simulation with the presence of a single rough particle, (b) the interference intensity $I_{\rm tot}$ recovered by Eq. (6), (c) the scattered-field intensity I_{zs} of Eq. (6), and (d) the intensity of the interference term I_{zi} in Eq. (6). The simulation results are also shown for the case of a random distribution of rough particles following the geometry shown in Fig. 3, as (e) Fourier transform amplitude of the scattered-field intensity I_{zs} and (f) Fourier transform amplitude of the interference term I_{zi}. The inset of (f) is the Fourier transform amplitude of the real part of the complex degree of coherence γ. In all cases, the refractive index of silicon with a carrier density $N = 3 \times 10^{21}$ cm^3, thus $\tilde{n} = 2.4 + 0.68i$ was used.

that comparing Fig. 10(d) with previously calculated energy absorption with the presence of multiple random roughness [Fig. 4(d)], we see identical energy absorption features in the frequency domain, except that Fig. 4(d) has more noise because of the multiple random roughness used in that calculation. Hence, the interference between scattered field caused by scattering centers of different locations should not play a role in the periodical energy modulations. To further elucidate this is indeed the case, we calculated the scattered field due

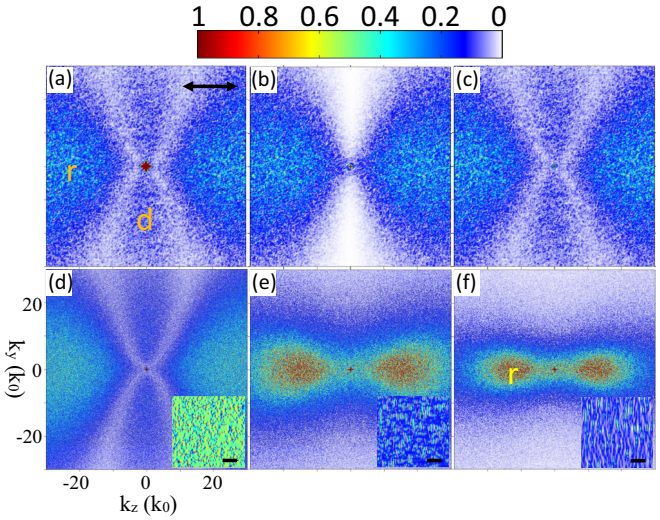

FIG. 11. (Color online) Fourier transform amplitude of (a) the total absorbed energy density $\xi = \xi_x + \xi_y + \xi_z$, (b) the interference term I_{zi}, and (c) the interference term plus the scattered term $I_{zi} + I_{zs} + I_{xs}$ at the depth $x = 0$ nm. The simulation was performed in plasmonic tungsten ($\epsilon_r = -10.5 + 16.4i$) with the presence of randomly distributed rough particles, following the geometry shown in Fig. 3. Multipulse simulations show the development of type-r feature in the Fourier transform of the energy absorption pattern after (d) the first pulse, (e) the third pulse, and (f) the fifth pulse. The insets are the corresponding energy absorption patterns in real space with the scale bar 200 nm. Note that, different from other calculations presented in this paper, rough particles of significantly smaller dimension are used.

to the presence of multiple random distributed roughness particles (following the geometry shown in Fig. 3). The Fourier transform amplitudes of the scattered-field intensity $|\mathrm{FFT}[I_{zs}]|$ and the interference intensity $|\mathrm{FFT}[I_{zi}]|$ are shown in Figs. 10(e) and 10(f), respectively. From the figure we can see that all the periodic energy modulation features (type-d, type-s, and type-r) we observed in Figs. 4(d)–4(f) are due to interference between the scattered field and the refracted field, i.e., the I_{zi} term of Eq. (6) [and also see the Fourier transform of γ in the inset of Fig. 10(f)]; the interference between the scattered field caused by different scattering centers gives negligible contribution to the final periodic energy modulations. It is worth noting that we further did simulations with an incident wave whose initial phase is a random function in the incident (y,z) plane or with an incident wave whose phase is randomly varying over the pulse duration, in both cases, the Fourier spectrum of the energy absorption shows no signature of periodical modulations, implying the determinant role of spatial and temporal coherence.

For metals, especially plasmonic metals, it is worth noting that the scattered field alone can also lead to inhomogeneous energy absorption. Figure 11(a) shows Fourier transform amplitude of the total absorbed energy of the three Cartesian components ($|\mathrm{FFT}[\xi = \xi_x + \xi_y + \xi_z]|$). The type-d feature is pronounced while in Fig. 11(b), which shows the Fourier transform of the interference term ($|\mathrm{FFT}[I_{zi}]|$), type d is missing. To investigate which field contributes to the type-d feature in this case, we retrieve the intensity of the other fields. Figure 11(c) shows the Fourier transform amplitude of the sum of the interference field I_{zi}, the z component of the scattered field I_{zs}, and the x component of the scattered field I_{xs}. The results are nearly identical to the Fourier transform of the total absorbed energy, implying the negligible contribution of the y component. Therefore, the type d in this case is attributed to the (near) scattered field only. Note that different from previous calculations, much smaller rough particles of height 5 nm and width 15 nm are used. The spatial frequency of smaller particles naturally has more overlap with high-frequency block (such as the type-r feature), thus enhancing the high-frequency components in the wave vectors of the scattered field, a requirement implied by the conservation of momentum. As a consequence, in Fig. 11, no type-s feature can be observed because its intensity is overwhelmed by the type-r features. Multipulse simulations (using the holographic ablation model which will be introduced in the next section and in Ref. [28]) show that in such a case, a steady growth of HSFLs perpendicular to the laser polarization (type-r) is allowed [see Figs. 11(d)–11(f)], is consistent with Ref. [28]. The periodicity is approaching $\Lambda \approx \lambda/12$ after five pulses [Fig. 11(f)], far beyond the diffraction limit. The small rough-particle dimension implies that laser fluence just above the material damage threshold should be beneficial to the formation of HSFLs beyond the diffraction limit. This is because fluence significantly higher than the threshold tends to produce deep valleys or large debris which effectively act as rough particles of larger dimension, initiates the otherwise type-s feedback trajectory (next section). This can be corroborated by the experimental result shown in Fig. 1(d) that HSFLs are seen on the edges of the focal spot where local fluence is low, while LSFLs are visible in the central area where local fluence is higher. This perhaps is also the reason that HSFLs are rarely seen using picosecond and nanosecond pulses since the process of longer pulse ablation is less deterministic as ultrafast laser ablation, thermal effects and large crack may develop which also act as large-dimension surface roughnesses, hindering the feedback path towards HSFLs beyond the diffraction limit.

E. Interpulse feedback and the formation of grooves

The question of a dynamic surface topography and LIPSS periodicity evolution with the irradiation dose is intrinsically related to the nature of the feedback. This includes a strong interrelation between the field and the topography and several hypotheses including plasmonic contribution, effective optical indices of corrugates surfaces or plasma gradients were proposed [24,33,46]. The full development of stable ripple patterns usually requires multiple laser pulses irradiate at the same spot. After the first few pulses, a premature ripple pattern forms on the surface, leading to valleys and ridges on the surface morphology. The following laser pulses interact with a revised surface, whose Fourier components in the frequency domain show distinct features, thus inevitably influences the wave vectors of the scattered field, leading to positive or negative feedbacks via the refractive index of the irradiated material [47]. A great advantage of FDTD over analytical models is that it has the ability to solve Maxwell's equations in a medium with arbitrary geometry, thus it has the potential to simulate interpulse feedback effect. We will

show that the feedback relates directly to the scattered field on topographically evolving surfaces.

The dynamical electron-phonon relaxation processes, the following transport of molten or ablated material, and resolidification which could lead to stable ripple patterns after the absorption of the laser pulses are complex and out of scope of this paper. The goal of this section is to illustrate the interpulse feedback mechanisms when all of those dynamical processes are over and to separate the contribution of the scattered field and the interference field on the enhancement of the ripple patterns. Therefore, we use a simple, so-called "holographic ablation model (HAM)" introduced by Skolski *et al.* [28]. The basic idea behind HAM is as follows. Before FDTD simulations of multiple pulses interacting with a rough surface, a FDTD simulation with identical parameters is used to calculate the absorbed energy below a flat surface without any roughness. It is therefore assumed that the threshold energy which leads to material removal of a layer thickness of Δx is the calculated energy absorption at a depth of $x = -\Delta x$ beneath the surface. Such a value of threshold energy is stored and used as the ablation threshold for the determination of material removal of the following pulses which interact with a rough surface. It should be noted that such a model neglects all the intrapulse effects, i.e., the change of material optical properties induced by the laser pulse, for example, Drude absorption in the case of excited semiconductors or nonplasmonic to plasmonic transitions. Hence, the ablation threshold in HAM is not required to be physical, its value could be arbitrary depending on the value of the incident field. Such an approach is satisfactory since it only accounts for the feedback mechanisms qualitatively.

Figure 12 shows the Fourier transform amplitude of the interference term I_{zi} and the scattering term I_{zs} in excited tungsten, obtained with the help of the HAM. As shown in Fig. 12(c), the laser pulse initially interacts with a surface with random roughness, and after several pulses, as shown in Figs. 12(f) and 12(i), LSFLs with a periodicity ~630 nm develop and enhance at higher number of pulses. The results agree with experiments well, as shown by the Fourier transform amplitude of the scanning electron microscopy image (SEM) in the up-corner inset of Fig. 12(i), where 80-fs laser pulses were used to produce the ripples on a tungsten sample. It is shown in Fig. 12(b) that the intensity of the scattered field is small and more or less equally distributed in all directions. It is the interference term I_{zi} that, as shown in Fig. 12(a), leads to initial inhomogeneous energy absorption responsible for the LIPSSs. Nevertheless, this is not true after the first pulse, as shown in Figs. 12(e) and 12(h), the scattering term I_{zs} shows type-s features at higher number of pulses. By a careful examination of the optical intensity in the real space and its comparison with the surface topography, it is found that, the optical intensity in the valleys are always larger than the intensity in the ridges, thus deepening the valleys through near-field enhancement, and hence leading to the enhancement of the ripple patterns (positive feedback). This positive feedback develops stable ripple patterns following the initial energy absorption with distinct Fourier components, and this revised surface roughness will in turn enhance the magnitude of the wave vectors of the scattered field at those distinct Fourier components. The scattered field with

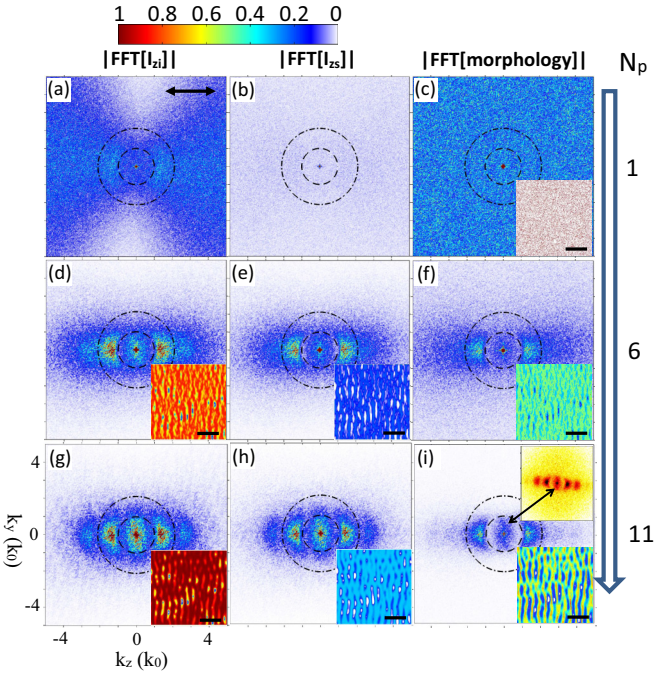

FIG. 12. (Color online) Interpulse feedback simulation of the formation of LIPSSs in plasmonic-active tungsten ($\epsilon_r = -10.5 + 16.4i$), illuminated by 11-fs laser pulses. (a), (d), (g) The Fourier transform amplitude of the intensity caused by the interference term I_{zi}. (b), (e), (h) The Fourier transform amplitude of the scattered-field intensity I_{zs}. (c), (f), (i) The Fourier transform amplitude of the surface morphology, before the 1st, the 6th, and the 11th pulses which are indicated by N_p. These surface morphologies are used to calculate the corresponding scattered field, hence obtaining I_{zi} and I_{zs}. The down-corner inset in each subfigure is the real-space pattern of the corresponding quantities with the scale bars 2 μm. The up-corner inset of (i) is the FFT of the SEM image of experimentally obtained ripple structure produced by 80-fs pulses in tungsten.

those enhanced wave vectors thus leads to a more efficient interference strength with the refracted field, giving rise to enhanced stable ripple patterns. It is worth noting that for high number of pulses, energy absorption pattern (HSFLs) with a periodicity approximately half of the LSFLs periodicity appears [see Figs. 12(g) and 12(h)], which seems to suggest the "ridge splitting" scenario [48–50], nevertheless, its origin deserves further study. The dependence of the periodicity of LSFLs on the pulse number applied has been studied for various materials in the literature and the general trend is that the periodicity decreases as the applied pulse number increases. According to Huang *et al.* [12], the decrease of periodicity is attributed to an increase of SPPs wave vector caused by a deepening gratinglike LSFLs structure. Our feedback simulations nevertheless do not support this grating-assisted SPP-laser coupling explanation. This is because that even for nonplasmonic tungsten which does not support the propagation of SPPs, the simulation shows qualitatively the same feedback results, ruling out the determinant role of SPPs. It is worth noting that other work which does not support the grating-assisted SPP-laser coupling hypothesis was found in the literature [28,51]. Our simulation, however, does not show

observable periodicity decrease on the 11 pulses investigated. As discussed by Oboňa *et al.* [51] and Skolski *et al.* [28], it could be due to the following reasons found in the literature: (1) In our simulations, a quasi-plane-wave with uniform intensity is used as the incident wave, thus, possible effects such as the change of the angle of incidence as the ablated crater deepens due to the Gaussian profile of the beam are not included in the calculations. As shown by Sipe *et al.* [19], the angle of incidence affects the periodicity of LSFLs. (2) A lack of transient variation of the refractive index in the calculations. The decrease of the excitation level (thus refractive index variation) from the center to the edge of the focused spot with a Gaussian profile is not included. Such a refractive index variation is a possible hypothesis in the literature to explain the pulse-number-dependent periodicity [22,28,51].

Aside from the LSFLs, it is also found from the simulation results that energy deposition with a periodicity larger than the laser wavelength is allowed for higher number of pulses. This can be seen clearly in the Fourier transform amplitude shown in Figs. 12(d)–12(i), for $N_p > 5$, as the amplitude of the Fourier transform for $|\mathbf{k}| < k_0$ shows an elliptical shape and is elongated in the direction along the K_y axis. This means that in real space, energy deposition with periodicities larger than the laser wavelength and orientated along the laser polarization is allowed [see Figs. 1(b) and 1(e) for examples]. Such a wavylike structure, often being referred as grooves, is actually what is observed experimentally in the up-corner inset of Fig. 12(i) and in Refs. [22,52]. The simulated surface morphology after 10 shots as shown in Fig. 12(i) almost fully reproduced the experimental data in tungsten as shown in the up-corner inset of Fig. 12(i) (note the double-sided arrow pointing out the experimental data and simulation of the grooves). Note both from the experimental fact and our simulations that the periodicity of the grooves in tungsten does not have a defined value; instead, it has a range of frequencies which can take any values from $k = 0$ to k_0. In other material or experimental conditions, the grooves can otherwise take the form of a very defined and organized structure [see, for example, Fig. 1(e)], which may have a different origin and it requires further study. The fact that FDTD simulations agree well with the experimental data in tungsten suggests a possible electro-magnetic contribution for the grooves, nevertheless, other contributions in the framework of hydrodynamic effects such as convection rolls [53,54] are reported. In this paper, we aim at calculating the energy absorption until the end of the pulse, no physical effects after the pulse end are included, therefore, only electromagnetic contribution of the grooves can be provided. Skolski *et al.* [55] calculated the inhomogeneous energy absorption under rough surfaces with a Gaussian frequency spectrum by the FDTD method. It was found that the exact spectrum of the rough surfaces affects the energy absorption responsible for the grooves. Here, we use a similar approach. Figure 12 shows that grooves appear only for higher number of pulses ($N_p > 5$) when the LSFLs have already developed. Therefore, it is not clear whether a corrugate surface is a precondition for the growth of grooves. This issue could be investigated by addressing the following question: Could a single (with topological symmetry) rough particle already show "groovelike" energy absorption features? Figure 13 illustrates just this, which shows the contour map

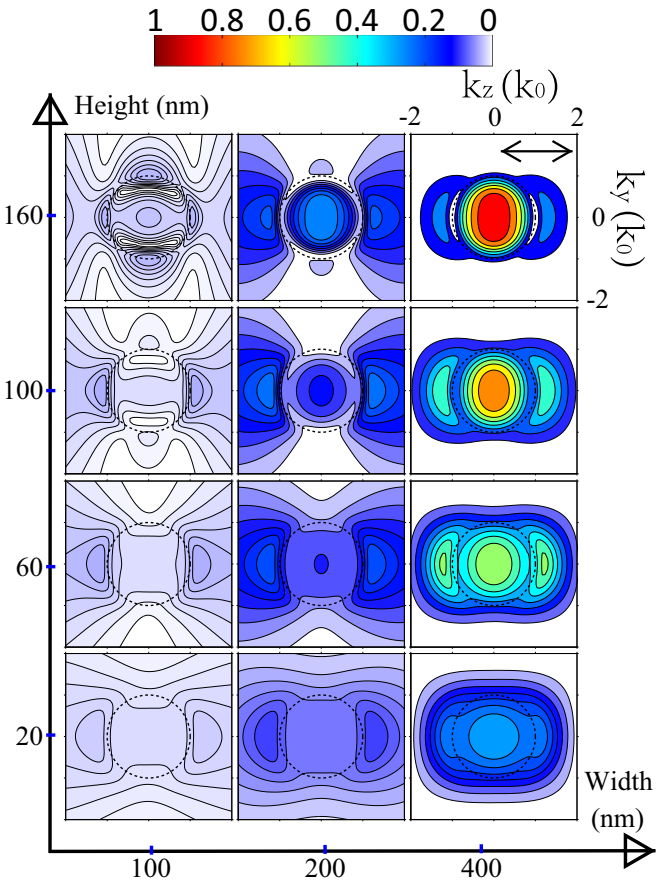

FIG. 13. (Color online) Contour map of the Fourier transform amplitude of the interference term I_{zi}, calculated under the presence of a single rough particle with a cubic shape, following the geometry shown in Fig. 6. The results are presented as a function of the width and the height of the rough particle (20, 60, 100, and 160 nm for height and 100, 200, and 400 nm for width). Each subfigure is placed at the corresponding quadrant in the "height-width" coordinate. The dashed line circles represent $|\mathbf{k}| = k_0$. The dielectric constant of plasmonic-active tungsten ($\epsilon_r = -10.5 + 16.4i$) is used for the calculations.

of the Fourier transform amplitude of the interference term I_{zi} for a single rough-particle (cubic shape, Fig. 6) in plasmonic-active tungsten ($\epsilon_r = -10.5 + 16.4i$). The simulations were carried out as a function of the width and the height of the rough particle. The simulations, as shown in Fig. 13, suggest that "groovelike" energy absorption features which are parallel to the polarization, could be developed if the width and height of the rough particle are both large, as the cases for width $\geqslant$200 nm and height $\geqslant$100 nm. This suggests that the formation of grooves does not necessarily require a corrugate surface as a precondition since no corrugation is considered in the above calculations. However, we should point out that initial positive feedback effects are absolutely required for the growth of grooves via the deepening of the valleys and perhaps on the same time, elevation of the ridges, so as to satisfy the height $\geqslant$100 nm condition. In fact, in Fig. 12 the grooves only start to grow after the fifth pulse where the depth of the valley starts to be larger than 100 nm since we set in the simulation that a 20-nm thick layer is removed after

each pulse, revealing a remarkable agreement between the two calculations. Ryan *et al.* [56] have shown that a preexistence of stepped features can affect the orientation of the LIPSSs depending on the orientation of stepped features with respect to the laser polarization. In our situation, however, we start with a randomly distributed rough surface, thus, we argue (and also showed) that the formation of grooves is strongly related to the deepening of the valleys (or the elevation of the ridges) caused by the positive feedback effects, and its orientation should depend on the laser polarization, not necessarily the corrugation orientation as we have shown that a corrugate surface is not a precondition. This of course cannot rule out the possibilities that a preexistence of corrugation surface affects the orientation of LIPSSs. Furthermore, because it is the interference term I_{zi} being calculated in Fig. 13, thus the interference between the (far) scattered field and the refracted field triggers the initial energy absorption patterns responsible for the grooves. The steady growth of grooves after initiation is the result of a feedback-driven topography evolution.

IV. SUMMARY

To summarize, we argue that the formation of organized nanostructures has an electromagnetic origin, triggered by a surface nanoscaled initial topography, without necessarily requiring collective charge oscillations sustaining propagative waves. This relation is sustained by the similarity of field spatial modulation along the surface and LIPSS for materials with various optical properties. Emphasizing the coherent character of interaction we demonstrate through an intuitive straightforward interference equation in combination with the FDTD calculated scattered field that the type-r feature (HSFLs perpendicular to the polarization) and the outer part of the type-d feature [HSFLs parallel to the polarization with $\Lambda < \lambda/\mathrm{Re}(\tilde{n})$] are initiated by coherent superposition between the usual refracted field and the scattered near field (evanescent), while the type-s feature (LSFLs perpendicular to the polarization) and the inner part of the type-d feature [HSFLs parallel to the polarization with $\Lambda > \lambda/\mathrm{Re}(\tilde{n})$] are initiated by coherent superposition between the usual refracted field and the scattered far field (propagation), although for plasmonic metals, the scattered near field alone could also contribute to HSFLs with $\Lambda < \lambda/\mathrm{Re}(\tilde{n})$ parallel to the polarization direction. Concerning the role of SPPs on the formation of LSFLs, we indicate the occurrence of a general light interference phenomenon that does not necessarily involve plasmonic excitation, materials which support plasmonic excitation only enhance the formation of LSFLs (type-s feature). For multipulse simulation of initially large-dimension rough particles, the results show an enhancement of LSFLs due to positive feedback and the growth of the grooves ($\Lambda > \lambda$), while initially small-dimension rough particles initiate the otherwise HSFLs (type-r) feedback path, which are both consistent with experimental results. It is also found that deepening of the valleys (or the elevation of the ridges) caused by the positive feedback effects are required for the formation of grooves, but it does not necessarily require a corrugate surface as a precondition since a single rough particle with symmetric geometry could already lead to "groovelike" energy absorption patterns. In general, the complexity of LIPSSs including LSFLs, HSFLs, and grooves is intrinsically initiated by the coherence of the laser field, via the coherent superposition between a topography-induced scattered field and the usual refracted field, and their steady growth after initiation is the result of a feedback-driven topography evolution.

ACKNOWLEDGMENTS

This work was supported by the French National Research Agency (ANR) project DYLIPSS (Project No. ANR-12-IS04-0002-01). C. Li acknowledges the financial support from China Scholarship Council. We are equally indebted to J. Tervo and O. Parriaux for their assistance in field coherence matters.

[1] J. L. Hansen, M. van Hecke, A. Haaning, C. Ellegaard, K. H. Andersen, T. Bohr, and T. Sams, Nature (London) **410**, 324 (2001).
[2] M. D. Betterton, Phys. Rev. E **63**, 056129 (2001).
[3] R. Cuerno, H. A. Makse, S. Tomassone, S. T. Harrington, and H. E. Stanley, Phys. Rev. Lett. **75**, 4464 (1995).
[4] M. A. Makeev, R. Cuerno, and A.-L. Barabasi, Nucl. Instrum. Methods Phys. Res., Sect. B **197**, 185 (2002).
[5] O. Varlamova, J. Reif, S. Varlamov, and M. Bestehorn, in *Progress in Nonlinear Nano-Optics* (Springer, Berlin, 2015), pp. 3–29.
[6] B. Öktem, I. Pavlov, S. Ilday, H. Kalaycıoğlu, A. Rybak, S. Yavas, M. Erdoğan, and F. O. Ilday, Nat. Photon. **7**, 897 (2013).
[7] M. Birnbaum, J. Appl. Phys. **36**, 3688 (1965).
[8] E. M. Hsu, T. H. R. Crawford, C. Maunders, G. A. Botton, and H. K. Haugen, Appl. Phys. Lett. **92**, 221112 (2008).
[9] Q. Wu, Y. Ma, R. Fang, Y. Liao, Q. Yu, X. Chen, and K. Wang, Appl. Phys. Lett. **82**, 1703 (2003).
[10] D. Dufft, A. Rosenfeld, S. K. Das, R. Grunwald, and J. Bonse, J. Appl. Phys. **105**, 034908 (2009).
[11] T. Q. Jia, H. X. Chen, M. Huang, F. L. Zhao, J. R. Qiu, R. X. Li, Z. Z. Xu, X. K. He, J. Zhang, and H. Kuroda, Phys. Rev. B **72**, 125429 (2005).
[12] M. Huang, F. Zhao, Y. Cheng, N. Xu, and Z. Xu, Phys. Rev. B **79**, 125436 (2009).
[13] V. Zorba, E. Stratakis, M. Barberoglou, E. Spanakis, P. Tzanetakis, S. H. Anastasiadis, and C. Fotakis, Adv. Mater. **20**, 4049 (2008).
[14] A. Y. Vorobyev, V. S. Makin, and C. Guo, Phys. Rev. Lett. **102**, 234301 (2009).
[15] B. Dusser, Z. Sagan, H. Soder, N. Faure, J. Colombier, M. Jourlin, and E. Audouard, Opt. Express **18**, 2913 (2010).
[16] R. Buividas, M. Mikutis, and S. Juodkazis, Prog. Quantum Electron. **38**, 119 (2014).
[17] E. M. Hsu, T. H. R. Crawford, H. F. Tiedje, and H. K. Haugen, Appl. Phys. Lett. **91**, 111102 (2007).
[18] A. Weck, T. Crawford, D. S. Wilkinson, H. Haugen, and J. Preston, Appl. Phys. A **89**, 1001 (2007).
[19] J. E. Sipe, J. F. Young, J. S. Preston, and H. M. van Driel, Phys. Rev. B **27**, 1141 (1983).

[20] J. Bonse, A. Rosenfeld, and J. Krüger, Appl. Surf. Sci. **257**, 5420 (2011).
[21] J. Bonse, A. Rosenfeld, and J. Krüger, J. Appl. Phys. **106**, 104910 (2009).
[22] J. Bonse and J. Krüger, J. Appl. Phys. **108**, 034903 (2010).
[23] M. Couillard, A. Borowiec, H. K. Haugen, J. S. Preston, E. M. Griswold, and G. A. Botton, J. Appl. Phys. **101**, 033519 (2007).
[24] M. Huang, Y. Cheng, F. Zhao, and Z. Xu, Ann. Phys. (NY) **525**, 78 (2013).
[25] J. P. Colombier, F. Garrelie, N. Faure, S. Reynaud, M. Bounhalli, E. Audouard, R. Stoian, and F. Pigeon, J. Appl. Phys. **111**, 024902 (2012).
[26] J. P. Colombier, F. Garrelie, P. Brunet, A. Bruyère, F. Pigeon, R. Stoian, and O. Parriaux, J. Laser Micro/Nanoeng. **7**, 362 (2012).
[27] G. D. Tsibidis, M. Barberoglou, P. A. Loukakos, E. Stratakis, and C. Fotakis, Phys. Rev. B **86**, 115316 (2012).
[28] J. Z. P. Skolski, G. R. B. E. Römer, J. V. Obona, and A. J. H. in 't Veld, J. Appl. Phys. **115**, 103102 (2014).
[29] J. Reif, F. Costache, M. Henyk, and S. V. Pandelov, Appl. Surf. Sci. **197–198**, 891 (2002).
[30] F. Costache, S.Kouteva-Arguirova, and J. Reif, Appl. Phys. A **79**, 1429 (2004).
[31] F. Costache, M. Henyk, and J. Reif, Appl. Surf. Sci. **208–209**, 486 (2003).
[32] J. Z. P. Skolski, G. R. B. E. Römer, J. V. Obona, V. Ocelik, A. J. Huis in't Veld, and J. Th. M. De Hosson, Phys. Rev. B **85**, 075320 (2012).
[33] S. Sakabe, M. Hashida, S. Tokita, S. Namba, and K. Okamuro, Phys. Rev. B **79**, 033409 (2009).
[34] M. Huang, F. L. Zhao, Y. Cheng, N. S. Xu, and Z. Z. Xu, ACS Nano **3**, 4062 (2009).
[35] W. Zhang, G. Cheng, X. D. Hui, and Q. Feng, Appl. Phys. A **115**, 1451 (2013).
[36] J. Tervo, T. Setälä, and A. Friberg, Opt. Express **11**, 1137 (2003).
[37] K. Yee, IEEE Trans. Antennas Propag. **14**, 302 (1966).
[38] D. M. Sullivan, *Electromagnetic Simulation Using the FDTD Method* (Wiley, Hoboken, NJ, 2000).
[39] M. Born and E. Wolf, *Principles of Optics* (Cambridge University Press, Cambridge, 1999).
[40] H. Zhang, S. A. Wolbers, D. M. Krol, J. I. Dijkhuis, and D. van Oosten, J. Opt. Soc. Am. B **32**, 606 (2015).
[41] K. Sokolowski-Tinten and D. von der Linde, Phys. Rev. B **61**, 2643 (2000).
[42] E. Bevillon, J. P. Colombier, V. Recoules, H. Zhang, C. Li, and R. Stoian, arXiv:1509.03182v1.
[43] A. D. Rakic, A. B. Djurisic, J. M. Elazar, and M. L. Majewski, Appl. Opt. **37**, 5271 (1998).
[44] L. Novotny and B. Hecht, *Principles of Nano-Optics* (Cambridge University Press, Cambridge, 2006).
[45] G. Obara, N. Maeda, T. Miyanishi, M. Terakawa, N. N. Nedyalkov, and M. Obara, Opt. Express **18**, 27226 (2010).
[46] A. Y. Vorobyev, V. S. Makin, and C. Guo, J. Appl. Phys. **101**, 034903 (2007).
[47] A. A. Ionin, S. I. Kudryashov, S. V. Makarov, A. A. Rudenko, L. V. Seleznev, D. V. Sinitsyn, and V. I. Emel'yanov, Laser Phys. Lett. **12**, 025902 (2015).
[48] A. Pan, A. Dias, M. Gomez-Aranzadi, S. M. Olaizola, and A. Rodriguez, J. Appl. Phys. **115**, 173101 (2014).
[49] J.-W. Yao, C.-Y. Zhang, H.-Y. Liu, Q.-F. Dai, L.-J. Wu, S. Lan, A. V. Gopal, V. A. Trofimov, and T. M. Lysak, Opt. Express **20**, 905 (2012).
[50] W. Zhang, G. Cheng, Q. Feng, L. Cao, F. Wang, and R. Hui, Appl. Surf. Sci. **257**, 4321 (2011).
[51] J. V. Oboňa, J. Z. P. Skolski, G. R. B. E. Römer, and A. J. Huis in't Veld, Opt. Express **22**, 9254 (2014).
[52] J. Bonse, M. Munz, and H. Sturm, J. Appl. Phys. **97**, 013538 (2005).
[53] G. D. Tsibidis, C. Fotakis, and E. Stratakis, Phys. Rev. B **92**, 041405(R) (2015).
[54] Y. Han, X. Zhao, and S. Qu, Opt. Express **19**, 19150 (2011).
[55] J. Z. P. Skolski, G. R. B. E. Römer, J. V. Obona, V. Ocelik, A. J. Huis in't Veld, and J. T. M. De Hosson, J. Laser Micro/Nanoeng. **8**, 1 (2013).
[56] R. D. Murphy, B. Torralva, D. P. Adams, and S. M. Yalisove, Appl. Phys. Lett. **104**, 231117 (2014).